



ELSEVIER

Contents lists available at ScienceDirect

Journal of Molecular Liquids

journal homepage: www.elsevier.com/locate/molliq



Molecular insights into supercritical methane sorption and self-diffusion in monospecific and composite nanopores of deep shale



Fangtao Lyu ^{a,b}, Zhengfu Ning ^{a,b,*}, Shanshan Yang ^{a,b}, Zhongqi Mu ^{a,b}, Zhilin Cheng ^c, Zhipeng Wang ^{a,b}, Bei Liu ^d

^a State Key Laboratory of Petroleum Resources and Prospecting, China University of Petroleum (Beijing), Beijing 102249, PR China

^b Department of Petroleum Engineering, China University of Petroleum (Beijing), Beijing 102249, PR China

^c School of Petroleum Engineering, Xi'an Shiyou University, Xi'an 710065, PR China

^d State Key Laboratory of Heavy Oil Processing, China University of Petroleum (Beijing), Beijing 102249, PR China

ARTICLE INFO

Article history:

Received 19 February 2022

Revised 15 April 2022

Accepted 25 April 2022

Available online 29 April 2022

Keywords:

Organic and inorganic matters

Monospecific and composite nanopores

Shale gas sorption

Molecular thermodynamics

Self-diffusion

ABSTRACT

Up to now, a large number of studies have utilized various representative materials to approximate the replacement of shale and investigate the gas adsorption and diffusion behavior in various shapes of nanopores by means of molecular simulations. However, the study of methane sorption and self-diffusion behavior under high temperature and pressure reservoir conditions in deep shale is not clear. In this study, we first established montmorillonite (MMT), kerogen and MMT-kerogen composite slit nanopores using representative shale components of MMT and kerogen. On this basis, we investigated the methane sorption and self-diffusion characteristics employing the grand canonical Monte Carlo (GCMC) and equilibrium molecular dynamics (EMD) simulations. The results show that the differences in the molecular composition and structure of MMT and kerogen surfaces lead to stronger adsorption performance of MMT surface than kerogen in a single nanopore for the same conditions, which results in the inhomogeneity of spatial distribution of methane molecules in the pores. While the sorption capacity of the kerogen matrix is more potent than MMT due to its larger specific surface area (SSA). The smaller pores have stronger adsorption capacity compared to the larger pores. At the same time, the methane density profiles indicate that the adsorption of the MMT and kerogen in smaller pores is less differentiated. The methane sorption energy distribution and isosteric heat of sorption also mutually corroborate the more stable methane sorption at a higher pressure and smaller pores. The self-diffusion coefficient of methane in nanopores gradually decreases with increasing pressure, with a more pronounced variation at lower pressure. Pore surface roughness will hinder the diffusion of gas, and the closer the distance is, the more noticeable the effect will be. This study sheds light on the sorption and self-diffusion phenomena and difference of gas in monospecific and composite nanopores, which provides insights into the reserve evaluation and development of the deep shale gas reservoirs, and is further expected to furnish ideas for exploring the occurrence and transport characteristics of supercritical fluids on other composite nanomaterials.

© 2022 Elsevier B.V. All rights reserved.

1. Introduction

As the exploration and development of conventional oil and gas resources worldwide have led to a sharp decline in remaining recoverable reserves, there is an urgent demand to seek new energy sources. Shale gas is gradually gaining popularity as a typical unconventional gas resource for its abundant reserves, clean and efficient characteristics. However, studies have indicated that

the current global shale gas-producing block reservoirs are mostly in ultra-low porosity and permeability conditions [1–4]. And to realize the economic and practical development of shale gas, hydraulic fracturing plus horizontal well technology has become the most mature and effective development technology and means at present [5–7].

Shale reservoirs are dense, with many micro- and nano-pores [8,9], so it is extremely crucial to understand the gas state in them to guide the assessment of shale gas resources and the design of oilfield development plans. Unlike conventional sandstone reservoirs, shale is rich in organic matter owing to its unique generation and evolutionary environment [10,11]. The results of shale mineral

* Corresponding author at: State Key Laboratory of Petroleum Resources and Prospecting, China University of Petroleum (Beijing), Beijing 102249, PR China.

E-mail address: ningzhengfu313@163.com (Z. Ning).

composition analysis show that in addition to a large proportion of inorganic matter (such as quartz, montmorillonite, illite, etc.), shale also contains the most essential hydrocarbon producing parent material (i.e., kerogen). Studies acknowledged that shale gas inhabits mainly in free and adsorbed states in the reservoir pores [12–15]. Laboratory low-temperature nitrogen adsorption and carbon dioxide adsorption experiments have testified that kerogen has an extensive specific surface area due to its loose and porous structure with tiny pores [16–18]. The pore internal surface area can provide many adsorption sites for gas. In addition, the inorganic matter also provides a suitable environment for gas adsorption due to their small pore size [9]. Therefore, it is of great significance to investigate the state of gas adsorption in the organic and inorganic matters of shale matrix as a prerequisite and basis for gas effective exploitation.

Many scholars have carried out research works on the unique occurrence state of shale gas. For the moment, the most prevalent research method is the laboratory isothermal gas adsorption experiment. The isothermal adsorption curve can be obtained by measuring the gas adsorption amount of shale particles at different temperatures and pressures, which can further evaluate the gas adsorption performance of shale [19–21]. According to the previous studies, there are many factors affecting gas adsorption in shale, which can be mainly summarized into the following aspects. Firstly, shale gas adsorption has a consanguineous relationship with its pore structure. Some experimental studies have analyzed that due to the multiple micro- and nano-pores in shale matrix, the interaction potential between the adsorbed molecules and various parts of the micropore walls will be superimposed, leading to the higher gas adsorption energy and easier to adsorb gas. Therefore, the order of shale pore adsorption under high pressure is from micropores to mesopores, then to macropores. And the adsorption mode is from filled adsorption of micropores to single molecular layer adsorption of mesopores and macropores [12,19,22,23]. Moreover, the composition of the shale, such as the total organic matter content (TOC) and the percentage of clay mineral components, have a more noticeable effect on the adsorption. It has been proved that an increase in organic matter contents induces an increase in gas adsorption by shale. Further experimental results manifested that the gas adsorption capacity of type III kerogen was stronger compared to type I and II kerogens [24–26]. In addition, studies have showed that thermal maturity would influence the surface properties of kerogen, and type IIB, C and D would show different behavior [27,28]. On this basis, massive published studies have analyzed the competing adsorption phenomena of CH₄ and CO₂. The results shown that CO₂ is more easily adsorbed on pores surface than CH₄ with strong affinity, making it possible to develop shale gas with CO₂ injection and providing guidance for geological carbon storage (GSC) [19,29,30]. Shale reservoirs contain connate water and fracturing fluid will enter the shale matrix pores for the strong capillary force during hydraulic fracturing [5,31]. Experimental results manifested that the presence of water competes with gas for adsorption and can significantly reduce methane adsorption amount, and the reduction gradually increased with the increase of water content [32–35]. At present, the experimental research is limited by the high temperature and pressure of deep shale. For example, the average reservoir depth can reach 3500–4000 m in Northern Sichuan and Weiyuan shale blocks in Sichuan province, China. The reservoir temperature can be up to 120°C or higher, and the reservoir pressure is far beyond that of conventional shale reservoirs [36–38]. The methane will be in a supercritical state for these temperature and pressure conditions, making the gas storage and flow characteristics more complicated. Therefore, new methods and approaches are urgently needed to carry out the related research works.

In recent years, scholars have started investigating shale gas sorption and flow characteristics from different perspectives employing molecular simulation and molecular dynamics methods. One of the main segments in which the sorbent model should be chosen is to approximate the shale reservoir. Many studies replaced shale reservoir rocks with single clay minerals, such as quartz, montmorillonite (MMT) and illite, to address this issue. Sun et al. [39] studies the adsorption behavior of CH₄ and CO₂ in quartz nanopores by the GCMC and MD methods, and found that the degree of surface hydroxylation had significant contributions to the adsorption selectivity of CO₂ over CH₄. Wang et al. [40] explored the competitive adsorption of methane and ethane in the MMT slit nanopores, and the results suggested that the adsorption affinity of MMT for methane molecules was higher at higher pressures. On this basis many scholars have investigated the effect of pore properties on methane adsorption [41,42]. Meanwhile, different types of kerogen molecules were utilized instead of organic matter to construct pore models, and the effects of kerogen type and maturity on gas adsorption were investigated [43–46]. Guo et al. [44] investigated the adsorption and absorption behaviors by kerogen nanoslit and matrix employing the GCMC method, and the effects of aperture, temperature and humidity on gas sorption were studied. Afagwu et al. [43] evaluated the effect of gas adsorption on the diffusion tortuosity of shale organic matter by means of molecular simulation, and the results revealed that the interaction between methane and kerogen increased the tortuosity by a factor of 3.6. Furthermore, numerous studies combined molecular mechanics (MM), grand canonical Monte Carlo (GCMC) and molecular dynamics (MD) simulations to investigate the effects of CO₂ and H₂O on CH₄ adsorption at high temperature and pressure, as well as the multi-component problem [47–50]. A comprehensive analysis was also carried out from the thermodynamic and energetic perspectives, including the interaction between gas molecules and the interactions between gas molecules and pore walls. Nevertheless, the effect of the nature of the pore wall on methane sorption is not clear in the context of comparative analysis of the realistic shale pore structures.

In addition, methane will be in a supercritical state due to the high temperature and pressure environment in deep shale reservoirs. Although previous works have quantitatively characterized the gas occurrence state in single organic and inorganic nanopores. Nevertheless, the effect of pore surface properties on gas storage state characteristics in inorganic–organic composite nanopores under supercritical conditions in realistic shale reservoir has been poorly understood and still needs to be addressed by further investigation.

In this study, we first utilized the representative components of shale, MMT and kerogen, to establish microscale monospecific and composite slit nanopores. On this basis, we have simulated the sorption characteristics of methane in the monospecific and composite nanopores under high temperature and pressure conditions utilizing the GCMC method and investigated the effects of pressure, pore size and pore surface properties. Furthermore, we also investigated the self-diffusion of methane by equilibrium molecular dynamics (EMD) and analyzed the differences in the self-diffusion of methane in different reservoir states. The results obtained can help understand the characteristics of gas distribution and diffusion in complex pores of shale matrix under supercritical states and provide some theoretical guidance for the development of shale gas in the field and the enhancement of gas recovery. Moreover, the results of this work and some of the conclusions drawn can provide some guidance for the study of gas and other fluids distribution and transport in composite nanomaterials, which can further enlighten the related research works in other industries and fields.

2. Models and methods

2.1. Construction of simulation models

As can be seen from the mineral composition of the shale, the shale matrix can be classified into two categories: organic and inorganic matters. It is obvious from the scanning electron microscopy (SEM) image of the shale matrix (Fig. 1) that organic matter is randomly distributed in the shale matrix and surrounded by inorganic matter. In addition to organic and inorganic nanopores, and there are generally tiny gaps at the boundary between the two. Meanwhile, deep shale reservoirs are often endowed with a certain amount of primary water, and during the subsequent hydraulic fracturing process, the fracturing fluid will also be imbibed into the shale matrix under the strong capillary force on account of the ultra-small pore size. Due to the difference in physicochemical properties of organic and inorganic matters, they will also undergo different degrees of deformation under the influence of different formation stresses and water, resulting in more obvious demarcation zones (micro-fractures) in adjacent areas. The differences in the surface properties of organic and inorganic matter lead to complex sorption and flow characteristics of gases in the composite pores formed by them. Na-MMT occupies a significant proportion of shale clay minerals and is used in place of the inorganic fraction during model construction. Meanwhile, type II kerogens are representative of oil-rich organic matter deposited in marine anoxic environments and are considered to be the most common source of hydrocarbon resources in major oil and gas blocks in the world, such as Barnett shale in northern Texas, the Bakken shale in northern United States, and the Wufeng and Longmaxi Formation shales in southwestern China [42,51,52]. Therefore, the type IIA kerogen as a typical kerogen molecule was involved in the model construction as the organic matter fraction. In this paper, the structure of the kerogen was obtained from the study of Ungerer et al. [46], and its molecular formula is $C_{252}H_{294-N_6O_{24}S_3}$. The construction process of the MMT, kerogen and MMT-kerogen composite slit nanopore models is presented in Fig. 2. Firstly, the obtained kerogen molecule was geometrically optimized and energy-optimized to obtain the relaxed kerogen molecule. Subsequently, 10 relaxed kerogen molecules were randomly placed into an empty box with dimensions of $91.84 \times 91.84 \times 91.84 \text{ \AA}^3$ and a density of 0.1 g/cm^3 . The system containing kerogen molecules was annealed and optimized. The annealing cycle

consisted of five ramp-up processes and five ramp-down processes, where the target temperature was gradually increased from an initial temperature of 300 K to a maximum temperature of 800 K, then continued to ramp down. The simulations were performed in the NVT ensemble with a total annealing time of 2 ns and a timestep of 1 fs, and the temperature was controlled by the Nose thermostat. Then a series of model optimization steps were carried out to construct the kerogen matrix with a target density by improving the method provided by Collell [52] for the purpose of this study, as shown in Table 1. First, the model was subjected to a high-temperature relaxation at 800 K in the NVT ensemble. Subsequently, kinetic simulations were performed at 80 MPa and then at 800, 600, 400 and 300 K for the NPT ensemble. The pressure was controlled by the Berendsen method and the temperature was also controlled by the Nose thermostat. The simulation time for NVT and NPT ensembles were 400 and 500 ps, respectively. 1 ns NPT simulation was finally performed under typical deep shale reservoir conditions (403.15 K and 80 MPa). During the NPT simulation, the density variation of the kerogen matrix is presented in Fig. 3. As illustrated in Fig. 3, the box size of the kerogen matrix shrinks as the simulation progresses, and the final density of the simulated kerogen matrix was 1.15 g/cm^3 , which was close to the results of previous studies [4,53–55]. The unit cell of MMT was first constructed by referring to the position coordinates of the atoms provided in the work of Skipper et al [56]. The chemical formula of MMT unit cell is $\text{Na}_{0.75}(\text{Si}_{7.75}\text{Al}_{0.25})(\text{Al}_{3.5}\text{Mg}_{0.5})\text{O}_{20}(\text{OH})_4$. The Na-MMT supercell consisted of $8 \times 4 \times 1$ MMT unit cells along the x, y and z directions, respectively. And eight tetravalent Si atoms were replaced by trivalent Al atoms on the silico-oxygen tetrahedra and 16 trivalent Al atoms were replaced by divalent Mg atoms on the aluminum-oxygen octahedra [56,57]. In this way, 24 Na ions were introduced between the layers to balance the excess charges and make the model electrically neutral. Then, the MMT crystal was geometrically and energetically optimized to obtain a more stable conformation. Finally, the optimized MMT crystal was cleaved along the (001) crystal surface to obtain the cleavage plane, which was used to build the MMT and MMT-kerogen composite nanopores using the Build Layers method. The obtained kerogen matrix and MMT supercell were assembled in parallel, respectively, and the models were kinetically optimized at 900, 700, 500 and 300 K within the NVT ensemble. Both MMT and kerogen layers were kept fixed during the simulation, while the position of Na ions can be continuously changed. Thus, the MMT, kerogen and composite models with target pore sizes can be obtained, and the model-related parameters are shown in Fig. 4. The pore size of the formed slit nanopores is defined as the minimum vertical distance between the lowermost atom of the upper surface and the uppermost atom of the bottom surface.

2.2. Force field

The COMPASS (Condensed-phase Optimized Molecular Potentials for Atomistic Simulation Studies) force field is a widely used force field that can handle both organic and inorganic small molecules and macromolecular systems [48,58,59]. Consequently, this study selects the COMPASS force field to describe the interactions between methane molecules and kerogen or MMT. The van der Waals interactions are calculated using the Lennard-Jones 9–6 (LJ 9–6) potential energy function [60] with a cutoff radius of 15.5 Å. The electrostatic interactions between atomic pairs are calculated using the Coulomb function [61], as shown in Eq. (1). It has been shown through previous studies that this force field can be used to obtain more reliable simulation results when studying the properties of gases such as adsorption on organic and inorganic matters [44,48,62].

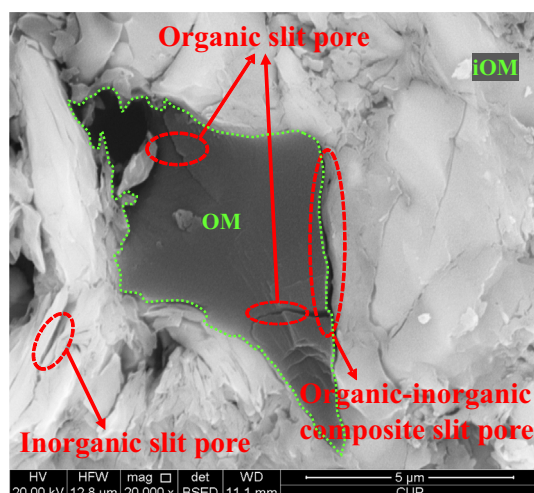


Fig. 1. Scanning electron microscopy (SEM) image of shale matrix.

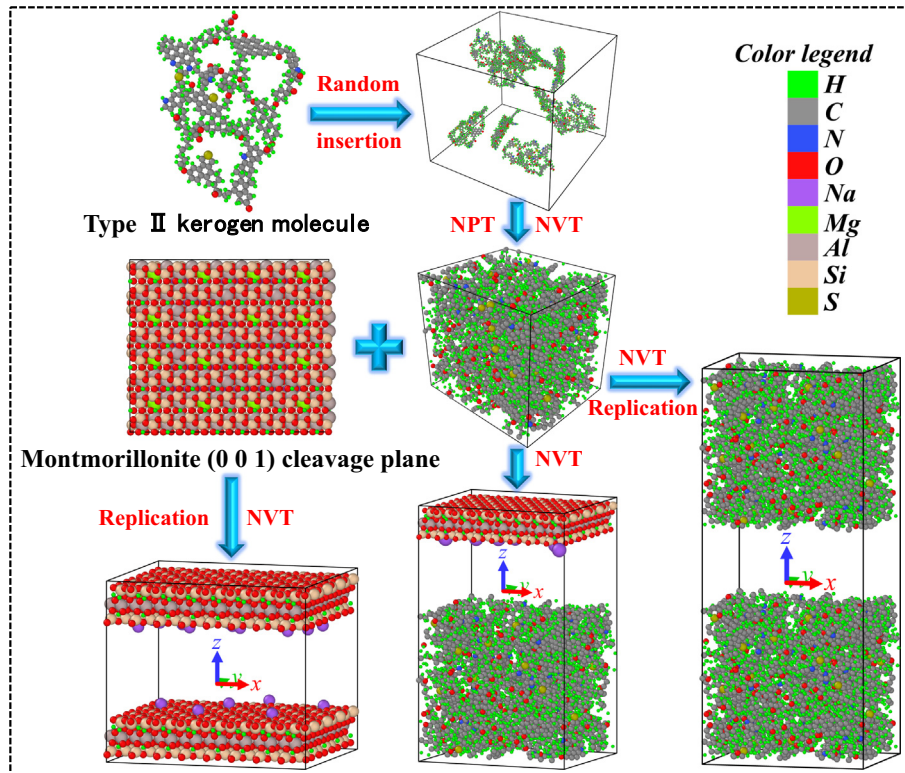


Fig. 2. Construction process of MMT, kerogen and MMT-kerogen composite slit nanopore models.

Table 1
NVT/NPT relaxation of the type IIA kerogen molecules for kerogen matrix construction.

Ensemble	T (K)	t (ps)	P (MPa)
NVT	800	400	\
NPT	800	500	80
NPT	600	500	80
NPT	400	500	80
NPT	300	500	80
NPT	403.15	1000	80

$$u(r_{ij}) = u_{ij} + u_C = \epsilon_{ij} \left[2 \left(\frac{r_{ij}^0}{r_{ij}} \right)^9 - 3 \left(\frac{r_{ij}^0}{r_{ij}} \right)^6 \right] + \frac{q_i q_j}{r_{ij}} \quad (1)$$

where r_{ij} denotes the distance between atoms i and j , q_i and q_j denotes the point charges carried by atoms i and j .

2.3. Simulation details

Firstly, the grand canonical Monte Carlo (GCMC) method were utilized to investigate the sorption behavior of methane molecules

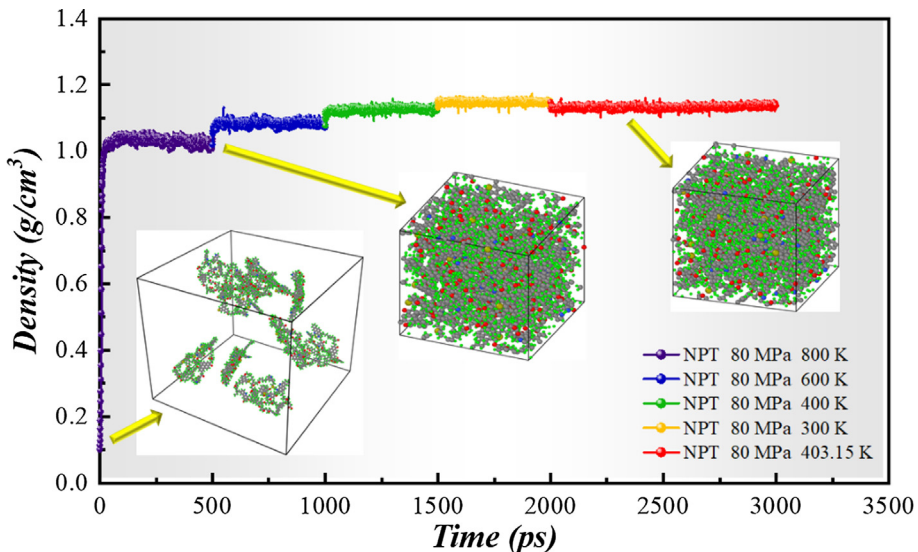


Fig. 3. The density variation of the kerogen matrix during the NPT dynamics optimization.

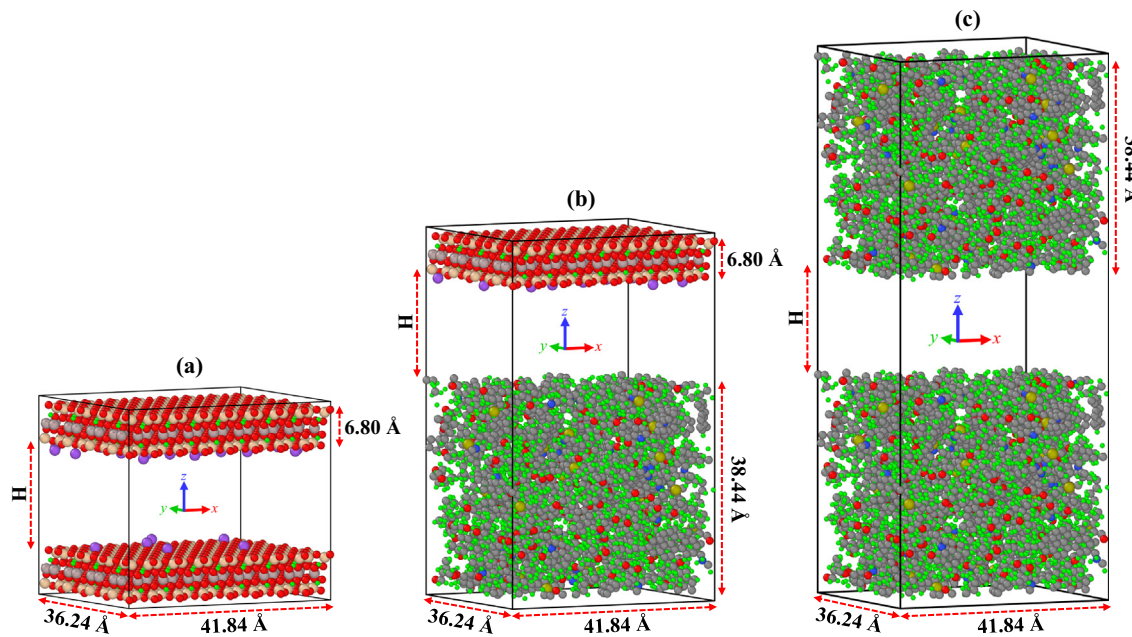


Fig. 4. The three simulation models with lattice-related parameters. (a) MMT model. (b) Kerogen model. (c) MMT-kerogen composite model.

in MMT, kerogen and MMT-kerogen composite slit nanopores, where the simulation boxes were set to periodic boundaries in the x, y and z directions. The isothermal sorption simulations were carried out in a typical deep shale temperature environment (403.15 K), and the pressure range is 1 to 80 MPa. Metropolis was chosen as the sampling method [63], Atom-based as the van der Waals summation method, Ewald as the electrostatic summation method. The temperature was controlled by the Nose-Hoover thermostat. For each pressure point, 2×10^6 Monte Carlo steps are performed to bring the simulated system to equilibrium, and then 2×10^6 steps were used as the production stage to obtain the sorption capacity. Methane gas physical parameters such as fugacity, bulk density were calculated by the NIST Standard Reference Database 23, using the REFPROP Version 9.0 software [64]. The methane fugacity and bulk density at different pressures are presented in Fig. 5.

Since the upper and lower surfaces of the constructed slit nanopores are uneven, and there are inaccessible regions for gas during the simulation. And helium is generally considered a non-adsorptive gas [65], so we adopted helium to calibrate the effective

volumes [66,67] of different nanopores at the condition of 403.15 K and 10 MPa, respectively. During all simulations, since the methane and helium molecules can enter the kerogen matrix through the pore surface, we only count the gas molecules in the main pore interspace and ignore the fraction that enters the kerogen matrix in the calculation [54,55]. Thus, the effective volume of the main pore is calculated by:

$$V_{p,\text{eff}} = \frac{zRT\langle N_{He} \rangle}{pN_A} \quad (2)$$

where z is the deviation factor of helium at the corresponding temperature and pressure conditions, R is the universal gas constant and takes the value 8.314 J/(mol·K), T is the simulation temperature. $\langle N_{He} \rangle$ denotes the average number of helium molecules in the main pore for given pore size, p denotes the simulation pressure, MPa, and N_A is Avogadro's constant and takes the value 6.022×10^{23} .

Based on the GCMC simulations, the generated configurations were continued to perform equilibrium molecular dynamics (EMD) simulations within the NVT ensemble with a simulation duration of 1 ns and a timestep of 1 fs to obtain more equilibrium configurations for analyzing the sorption and self-diffusion behavior of methane. When the EMD simulations reached about 200 ps, the system temperature and energy have basically stabilized, which means that the simulations were already in dynamic equilibrium. Therefore, we used the latter 750 ps of the simulations for data sampling and analysis. The system temperature was controlled by a Nose-Hoover thermostat. All simulation works were carried out by the Materials Studio software package, and the OVITO software [68] was used to launch the subsequent visualization and data processing.

3. Simulation validation

In our work, we constructed the kerogen matrix to approximate realistic organic matter of shale, due to the porous structure of kerogen, so we must verify the rationality of our model. In addition, the COMPASS force field was chosen to perform all the simu-

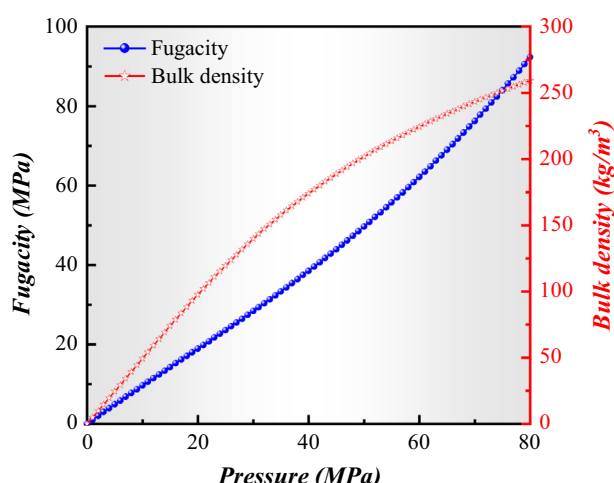


Fig. 5. Variation of methane fugacity and bulk density with pressure at 403.15 K.

lations, and the applicability of this force field to our model also should be validated.

3.1. Model validation

We employ the probe method proposed by Connolly [69] to investigate the pore structure characteristics of the kerogen matrix. Probe molecules with fixed radius are inserted randomly in the kerogen matrix, and the probe is rolled across the atomic van der Waals surface to determine the solid skeleton surface, the area covered by the skeleton surface is identified as free pore volume. When helium was selected as the probe molecule, the Connolly surface was formed as shown in Fig. 6. The porosity and specific surface area (SSA) of kerogen matrix detected by helium are 21.13% and $1704 \text{ m}^2/\text{g}$, respectively, which are very close to the experimental values and simulation results by other researchers [53,70]. Thus, the accuracy and rationality of the kerogen matrix model were well verified.

3.2. Force field validation

Appropriate force field parameters are a vital prerequisite for determining the reliability of simulation results. To this end, we compare the bulk density of methane calculated by NIST and the simulation results. The bulk density in the simulation results was obtained from the 4 nm nanopores of the MMT and kerogen models, respectively. The comparison results are presented in Fig. 7. As illustrated in Fig. 7, for both MMT and kerogen models, the simulation results are in good agreement with the calculation results, which demonstrates that the selected force field has good applicability to the simulation system.

4. Results and discussion

4.1. Methane sorption characteristics

4.1.1. Isothermal sorption of methane

To begin with, we investigated the adsorption behavior of methane in MMT, kerogen and MMT-kerogen composite slit nanopores under typical deep shale reservoir conditions (403.15 K), where the apertures are 1, 2 and 4 nm, respectively. Some studies have shown that the sorption of gas molecules in kerogen can lead

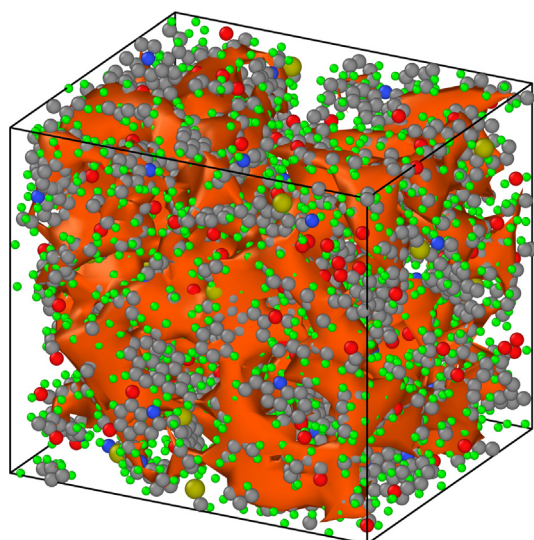


Fig. 6. The kerogen matrix model with Connolly surface. Jacinth represents the surface formed by the trace left by the rolling of the probe atoms.

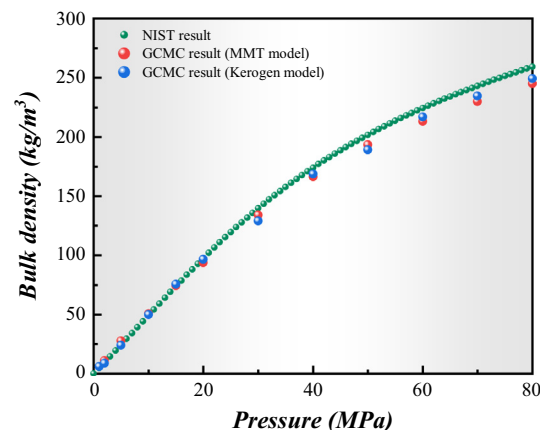


Fig. 7. Comparison between calculation and simulation results of methane bulk density.

to changes in the volume of kerogen, which is called swelling effect [30,71]. In our study, we only focused on the sorption of methane molecules by the kerogen, and did not consider the change of kerogen volume caused by the sorption. Therefore, all kerogen molecules were fixed during the simulation process. The excess and absolute adsorption of methane are the adsorption amounts corresponding to unit pore surface area [67], respectively. The excess adsorption amount in the slit nanopores can be obtained from Eq. (3).

$$n_{ex} = \frac{\langle N_{CH4} \rangle / N_A - \rho_b V_{p,eff} / M_{CH4}}{2S_A} \quad (3)$$

where n_{ex} denotes the methane excess adsorption capacity corresponding to unit pore surface area, mol/m^2 , $\langle N_{CH4} \rangle$ is the average number of methane molecules loading in the pore interspace during GCMC simulation, N_A is Avogadro's constant, which is 6.022×10^{23} . ρ_b is the bulk density of methane, g/cm^3 . $V_{p,eff}$ denotes the effective pore volume of the slit pore, cm^3 . M_{CH4} is the molar mass of methane, and S_A is the unilateral surface area of the slit pore, m^2 .

Furthermore, the absolute adsorption amount per unit surface area in the pores can be calculated by the excess adsorption [67].

$$n_{abs} = n_{ex} + \frac{\rho_b V_{ads} / M_{CH4}}{2S_A} \quad (4)$$

where n_{abs} denotes the absolute methane adsorption amount per unit pore surface area, mol/m^2 . V_{ads} is the volume of adsorbed phase in the pore, cm^3 , which can be calculated from the methane density profile.

Substituting Eq. (3) into Eq. (4), the absolute adsorption amount can be expressed as:

$$n_{abs} = \frac{\langle N_{CH4} \rangle / N_A + \rho_b (V_{ads} - V_{p,eff}) / M_{CH4}}{2S_A} \quad (5)$$

To compare the adsorption capacity of MMT and kerogen, and be consistent with the experimental results. We converted the absolute adsorption amount into the corresponding value per unit mass according to the relative mass of the model, respectively. Then Langmuir isothermal adsorption formula [72–74] was used to fit the absolute adsorption amount.

$$n_{abs} = n_L \frac{p}{p + p_L} \quad (6)$$

where n_{abs} denotes the absolute adsorption amount per unit mass, mol/g . n_L is the Langmuir adsorption amount, refers to the maximum adsorption capacity of monolayer, mol/g . p_L is the Langmuir

pressure, refers to the adsorption amount to reach the maximum adsorption capacity of half the corresponding pressure, MPa.

The adsorption isotherms in the MMT, kerogen and MMT-kerogen composite model nanopores at 403.15 K are presented in Fig. 8. As depicted in Fig. 8(a-c), the excess adsorption isotherms can be roughly divided into two stages. The first stage is a rapid rise from 1 to 20 MPa, and the slope of the curve in this stage is larger and belongs to the rapid adsorption stage. Due to the relatively small size of the studied pores, the adsorption layers occupy the pore interspace, and the gas adsorption reaches saturation. Therefore, in the second stage (20–80 MPa), as the pressure continues to rise, the bulk density continues to increase, resulting in a decreased trend in the excess adsorption amount. By comparing the three

curves for different apertures, it can be found that with the increase of aperture, the excess adsorption amount decreases. This shows that smaller pores have stronger gas adsorption performance, which is also widely reflected in previous studies [40,41,55]. However, 1 nm is too small compared to 2 nm, and the pore space for gas adsorption is insufficient, resulting in a slightly smaller excess adsorption amount than that of 2 nm. In all the three cases, methane adsorption is microporous and a larger aperture can provide more adsorption space. Therefore, the absolute adsorption amount increases with increasing aperture in the same condition of the three models. The absolute adsorption capacity of the 2 nm pore is slightly higher than that of 4 nm due to its stronger adsorption capacity. Meanwhile, the slope of

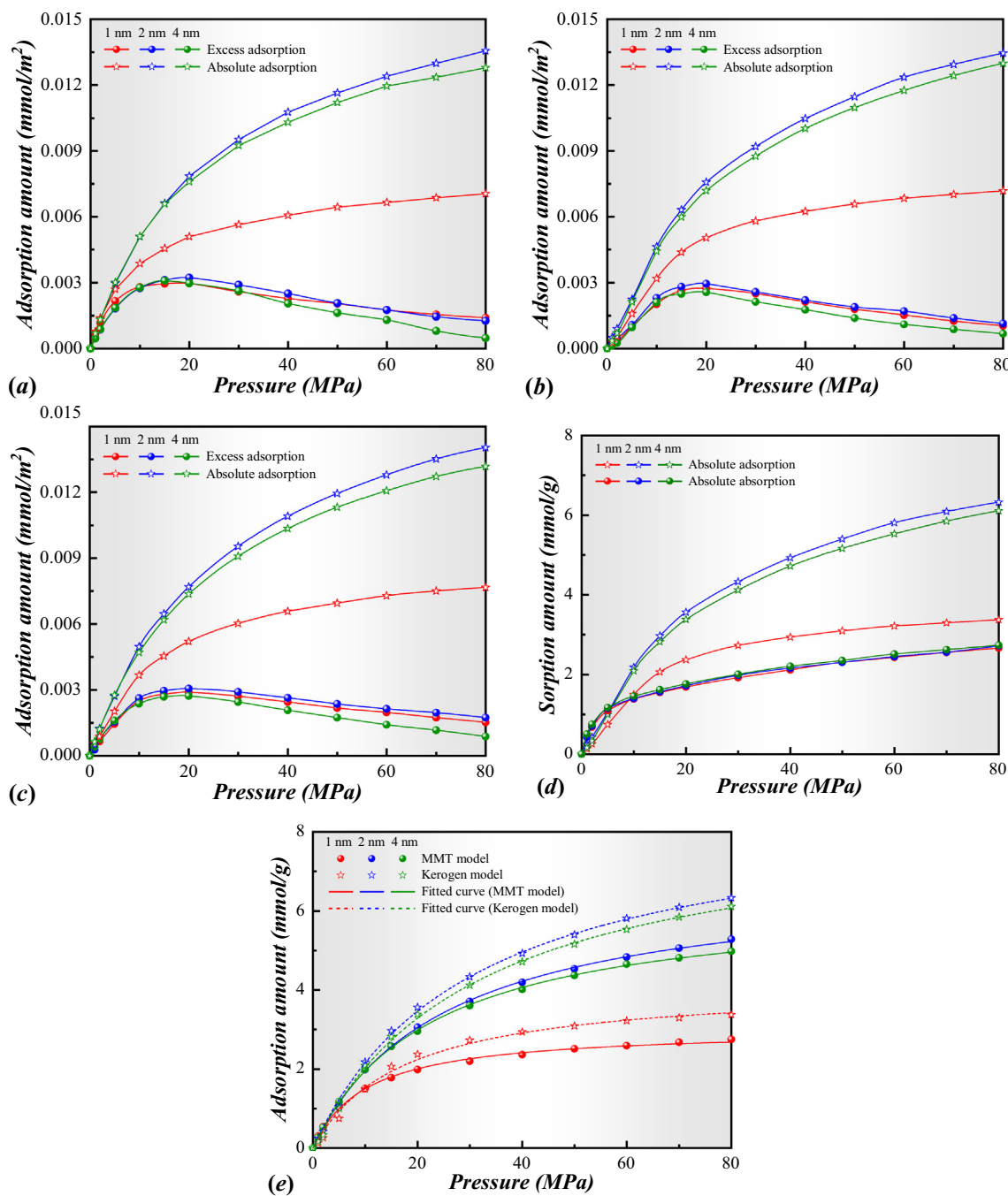


Fig. 8. Methane sorption isotherms at 403.15 K with different apertures. (a) MMT model. (b) Kerogen model. (c) MMT-kerogen composite model. (d) Absolute adsorption and absorption isotherms of kerogen models. (e) Langmuir fitting results of MMT and kerogen models.

the absolute adsorption curve shows that the rapid gas adsorption mainly occurs in the first half of the pressure change, while the gas adsorption slows down in the second half. With the further increase of pressure, the absolute adsorption amount will reach a peak, and no longer varies with pressure thereafter.

Meanwhile, comparing the methane adsorption in MMT, kerogen and MMT-kerogen composite model nanopores, it can be found that MMT surface has stronger adsorption performance than kerogen surface, while the MMT-kerogen composite nanopore is in between. This may be due to the loose and porous surface of kerogen matrix, which does not provide enough adsorption sites for methane. In addition, the surface inhomogeneity of kerogen is much stronger, leading to considerable uncertainty in methane adsorption. Since gas can enter the kerogen matrix during the simulation process, we calculated the adsorption and absorption isotherms of methane in the kerogen models. As shown in Fig. 8(d), the absolute adsorption amount of methane is greater than the absorption amount under the same conditions. Moreover, the absorption isotherms of methane for different apertures are almost overlapped, which further demonstrates the reliability of the simulation results. The sorption isotherms of the MMT and kerogen model nanopores per unit mass are presented in Fig. 8(e). As can be observed from the Fig. 8(e) that the methane absolute adsorption of the kerogen nanopore is greater than that of the MMT nanopore. Comparing with MMT, the specific surface area (SSA) of the kerogen matrix is larger, which can provide more adsorption sites for methane, resulting in a larger gas adsorption capacity. In addition, Langmuir isothermal adsorption was utilized to fit the absolute adsorption capacity of MMT and kerogen model nanopores, and the fitting results are presented in Fig. 8(e). It can be seen from the Fig. 8(e) that good fitting results were obtained. The fitting parameters are presented in Table 2. It can be seen from the Table 2 that the variation of maximum adsorption capacity (n_L) has a good agreement with the simulation results. Meanwhile, the Langmuir pressure (p_L) of kerogen is higher than that of MMT for the same pore size, indicating that the kerogen requires higher pressure to reach adsorption saturation, which is also consistent with the previous analysis.

4.1.2. Methane density distribution

To further understand the adsorption behavior of methane in MMT, kerogen and MMT-kerogen composite model nanopores, the sorption configurations in different pores at 403.15 K and 30 MPa are presented in Fig. 9. Since we only study the methane adsorption behavior in the slit pores, the carbon atoms in the methane molecules are represented in rose and hydrogen atoms in light blue to distinguish them. It can be seen from the Fig. 9 that methane molecules aggregate near the pore surfaces, and the molecular density is significantly larger than that of the pore center. At the same time, methane molecules are distributed more orderly on the surface of MMT compared to the surface of kerogen, which is highly related to the heterogeneity of the kerogen pore surface. Thus, we investigated the density distribution profiles of methane perpendicular to the pore surface in the three models for different pressures (1–80 MPa) and apertures (1, 2 and 4 nm).

As illustrated in Fig. 10(a, d), the methane density in the slit pores of the MMT and kerogen models increased continuously with increasing pressure at the pore size of 1 nm. With the increase of pressure, methane adsorbed and formed two strong adsorption layers on the top and bottom surfaces of the pore. And with the further increase of pressure, the density of gas adsorption layers also increases continuously. As shown in Fig. 10(g), the gas adsorption layer is formed on the MMT surface prior to the kerogen surface at low pressure, which further indicates that MMT has a stronger surface adsorption performance than kerogen in a single nanopore. It can be seen from the Fig. 10(a, d, g) that in the case of 1 nm, the double adsorption layer formed basically occupies almost all the space in the accessible area of the pore. In addition, a gas inaccessible region with a thickness of about 1 Å can be found on the surface of MMT. And since the methane can enter the kerogen matrix through the voids on the kerogen surface, there is a non-zero density value on the kerogen surface. As displayed in Fig. 10(b, e), when the aperture increased to 2 nm, a second adsorption layer weaker than the first was formed on the pore surfaces of MMT and kerogen nanopores with the increase of pressure. Henceforth, a four-adsorption-layer structure was formed in the pores, and the peak density of each adsorption layer increased continuously with the increase of pressure. As presented in Fig. 10(h), the second adsorption layer was formed on the MMT surface before that on the kerogen surface with the increase of pressure in the composite nanopore, and the density peak of the adsorption layer was larger. As the aperture increased by 4 nm, as illustrated in Fig. 10(c, f, i), methane four-adsorption-layer structure is also formed in the pores of the three models with increasing pressure. Comparing the variation of methane density profiles with pressure for different pore sizes, it can be found that the first and second adsorption layers are always formed earlier on the MMT side than on the kerogen side with the increasing pressure. That is, only lower pressure is required on the MMT side compared to the kerogen side to form corresponding adsorption layers, further indicating that the adsorption capacity of MMT surface is more robust than that of kerogen in a single nanopore.

To further investigate the effect of pore surface properties on gas adsorption, we analyzed the relationship between the density of different adsorption layers in the MMT-kerogen composite nanopores. Fig. 10(j) depicted the density distribution of methane at 30 MPa in the 2 nm composite nanopore. Firstly, we defined the adsorption peak closest to the kerogen side as the first adsorption layer, the one closest to the MMT side as the second adsorption layer, and the next closest adsorption peaks as the third and fourth adsorption layers. It can be seen from the Fig. 10(j) that the widths of these four adsorption layers are all approximately equal to the molecular diameter of methane, indicating that each gas adsorption layer is monolayer adsorption. Fig. 10(k) shows the methane density distribution of MMT and kerogen nanopores for different apertures at 30 MPa. It can be seen from the Fig. 10(k) that the density peaks of each adsorption layer decrease with the increase of aperture, indicating that the adsorption performance of smaller pores is stronger. Meanwhile, the peak density of the MMT model is significantly higher than that of the kerogen model for the gas

Table 2

The Langmuir fitting results of MMT and kerogen models with different apertures.

Model	Aperture (nm)	n_L (mmol/g)	p_L (MPa)	R^2
MMT	1	3.024	10.17	0.9982
	2	6.869	25.11	0.9998
	4	6.354	22.53	0.9998
Kerogen	1	4.172	17.24	0.9933
	2	8.736	30.44	0.9989
	4	8.484	31.61	0.9985

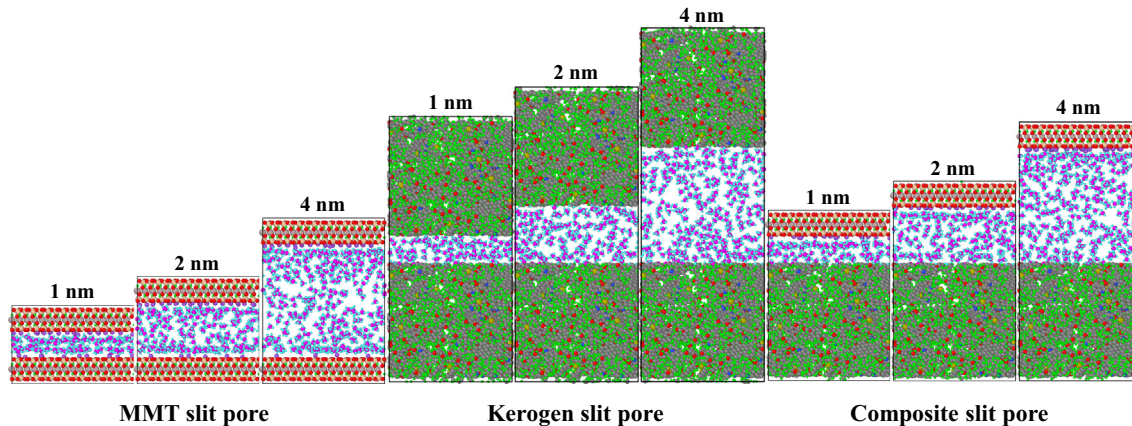


Fig. 9. Methane sorption configurations in MMT, kerogen and MMT-kerogen composite model nanopores for different pore sizes at 403.15 K and 30 MPa.

adsorption layer at the same location. In order to study the relationship between peak density of adsorption layer and surface properties, we counted the peak density of adsorption layer under different apertures in the composite nanopores at 30 MPa. As demonstrated in Fig. 10(l), the peak density of the adsorption layer on the side of the kerogen is smaller than that on the side of MMT for the same conditions. This indicates that the adsorption capacity of methane on the surface is greater than that kerogen, leading to the differential adsorption of the gas in the MMT-kerogen composite nanopores. To further reveal the relationship between this variability and pore size in the composite nanopores, we introduced the density difference ratio (R_p), which is defined as the ratio of the peak density between the first and second adsorption layers. It can be seen from the Fig. 10(l) that the density difference ratio decreases with the increasing aperture. This illustrates that the adsorption difference between MMT and kerogen is smaller in the smaller composite nanopores. However, in general, R_p is always a value less than 1, which also indicates that the adsorption capacity of MMT surface is stronger than that of kerogen in a single nanopore.

4.1.3. Energy density distribution of methane

In this section, the sorption behavior of methane in MMT, kerogen and MMT-kerogen composite model nanopores is further analyzed from an energetic point of view. During the simulation, the total energy of either sorption configuration is composed of both electrostatic force and van der Waals force [75].

$$E_T = E_{SS} + E_{SF} + U_S \quad (7)$$

where E_T is the total energy of the simulation system, kcal/mol. E_{SS} is the intermolecular energy of the adsorbate (methane), kcal/mol. E_{SF} denotes the interaction energy of the adsorbate and the adsorbent (MMT or kerogen), kcal/mol. U_S is the total internal energy of the adsorbent, kcal/mol.

Since MMT and kerogen remain rigid throughout the simulation, so the interaction energy between adsorbent will not be included anymore. That is, only the first two terms on the right side of the equation are considered in Eq. (7). Where the change in the distribution of the interaction energy between adsorbate and adsorbent during the sorption simulation process can be described by the sorption energy distribution curve.

The energy distribution curves of methane sorption in the MMT, kerogen and MMT-kerogen composite models with aperture of 1, 2 and 4 nm are presented in Fig. 11. And the data for remaining pressure points are shown in Fig. S1 of the Supporting Information. As illustrated in Fig. 11(a), the energy distribution curves of methane sorption in MMT model with an aperture of 1 nm exhibit a single

peak. And the curve shifts to the right with the increase of pressure, which shows that the sorption gradually shifts from high-energy (absolute value) sorption sites to low-energy (absolute value) sorption sites, indicating that the methane sorption is more stable at higher pressure. As shown in Fig. 11(d, g), the energy distribution curves of sorption in kerogen and MMT-kerogen models with the aperture of 1 nm exhibit a double peak, indicating that sorption is divided into two interaction regions. This is because methane will enter the kerogen matrix through the voids on the surface of kerogen during the simulation, and the sorption in the main pores of the models and the kerogen matrix will be different. At the same time, due to the different interactions between adsorbents (MMT and kerogen) and methane, which leads to the difference of energy distribution curves. As presented in Fig. 11(d), the amplitude of the high energy peak (absolute value) on the left side decreases with increasing pressure, while the low energy peak (absolute value) on the right shifts left and the amplitude increases, and the energy distribution curve becomes nearly single peak at high pressure. It indicates that the variability of methane sorption in the main pore of the model and shale matrix is getting smaller as the pressure increases. As displayed in Fig. 11(g), since the MMT surface has stronger adsorption sites relative to the kerogen, resulting in the methane adsorbed by MMT possessing lower potential energy, which is shown in the figure as the amplitude of the high energy peak (absolute value) on the left is smaller than the lower energy peak (absolute value) on the right. In addition, the high energy peak (absolute value) on the left shifts slightly to the right and the low energy peak (absolute value) on the right shifts to the left, and becomes almost a single peak at high pressure. As illustrated in Fig. 11(b, c), the energy distribution curves of sorption in the MMT models with apertures of 2 and 4 nm show double peaks, which is also consistent with the bilayer sorption structure of the pore surface. With the increase of pressure, both energy peaks shift to the left, indicating that methane sorption gradually shifts from high energy (absolute value) sorption sites to low energy (absolute value) sorption sites, and methane sorption is more stable under higher pressure. As shown Fig. 11(e, f), the energy distribution curves of sorption in the kerogen models with apertures of 2 and 4 nm exhibit double peaks. Besides being influenced by the bilayer adsorption on the kerogen surface, methane sorption is still mainly divided into the adsorption in the main pore and the absorption in the kerogen matrix. Moreover, the difference between the two sorption keeps getting smaller as the pressure increases. As shown in Fig. 11(h, i), the energy distribution curves of sorption in the MMT-kerogen composite model with apertures of 2 and 4 nm exhibit three peaks. With the increase of pressure, the two low energy peaks (absolute value)

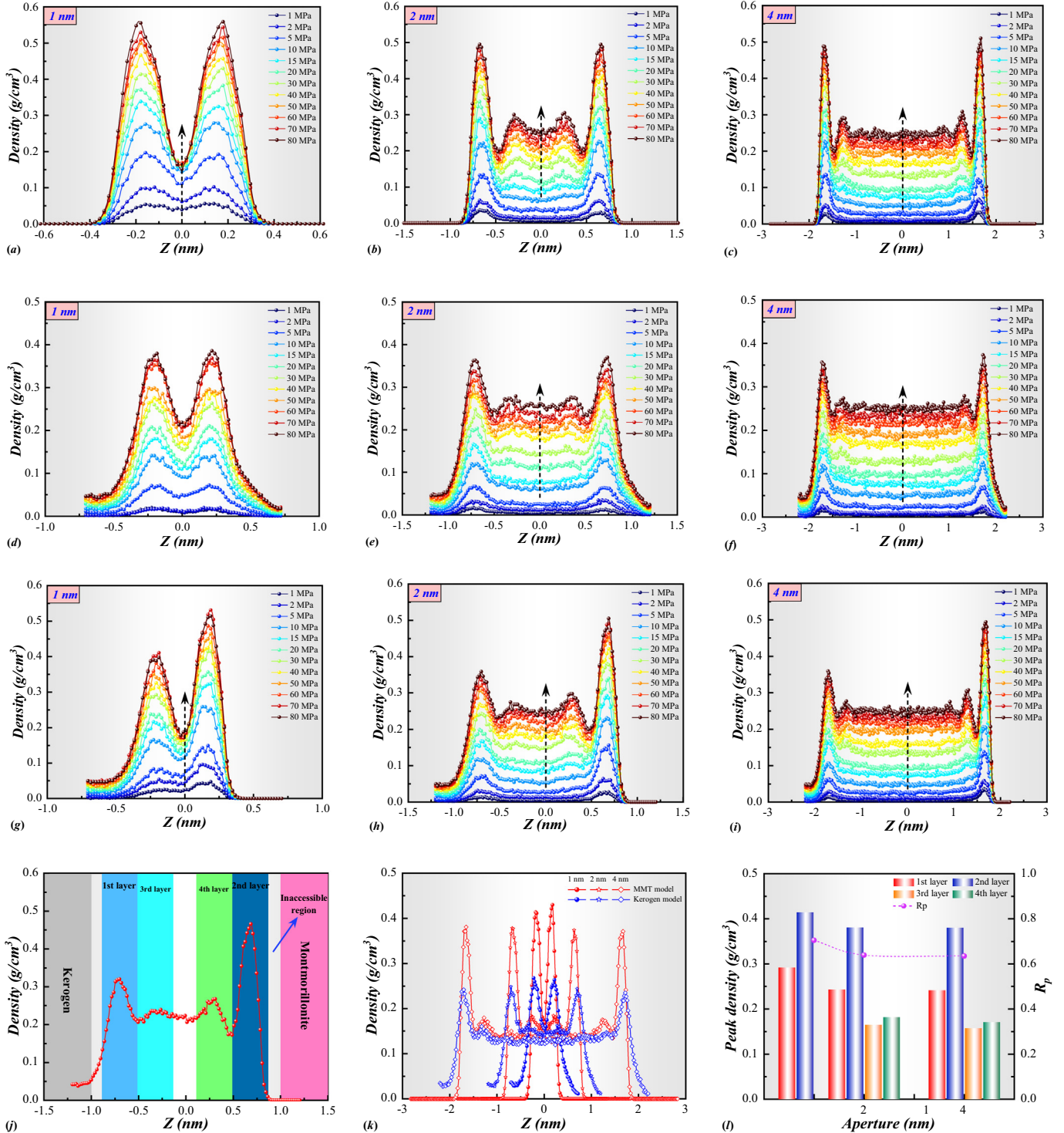


Fig. 10. Density distribution of methane in nanopores of the three models with the apertures of 1, 2 and 4 nm. (a-c) MMT model. (d-f) Kerogen model. (g-i) MMT-kerogen composite model. (j) Methane density profile stratification in MMT-kerogen composite nanopore. (k) Variation of methane density profiles with pore size in MMT and kerogen nanopores at 30 MPa. (l) Variation of methane peak density of each adsorption layer and density difference ratio with pore size in MMT-kerogen composite nanopores at 30 MPa.

on the right shift to the left, while the amplitude of the high energy peak (absolute value) on the left decreases, and the curves present an approximate single-peak state under high pressure. It shows that the sorption is more stable with the increase of pressure in the composite model, and the difference of sorption between MMT and kerogen becomes smaller. Fig. 11(j) depicts the energy distribution curves of sorption in the three models at 30 MPa for

apertures of 1, 2 and 4 nm, respectively. As can be seen from the Fig. 11(j) that the energy distribution curves of sorption shift to the right with increasing aperture, that is, the interaction energy decreases. It indicates that the sorption gradually shifts from lower energy (absolute value) sorption sites to the higher as the aperture increases, which further demonstrates that smaller pores have stronger adsorption capacity than larger pores. Meanwhile,

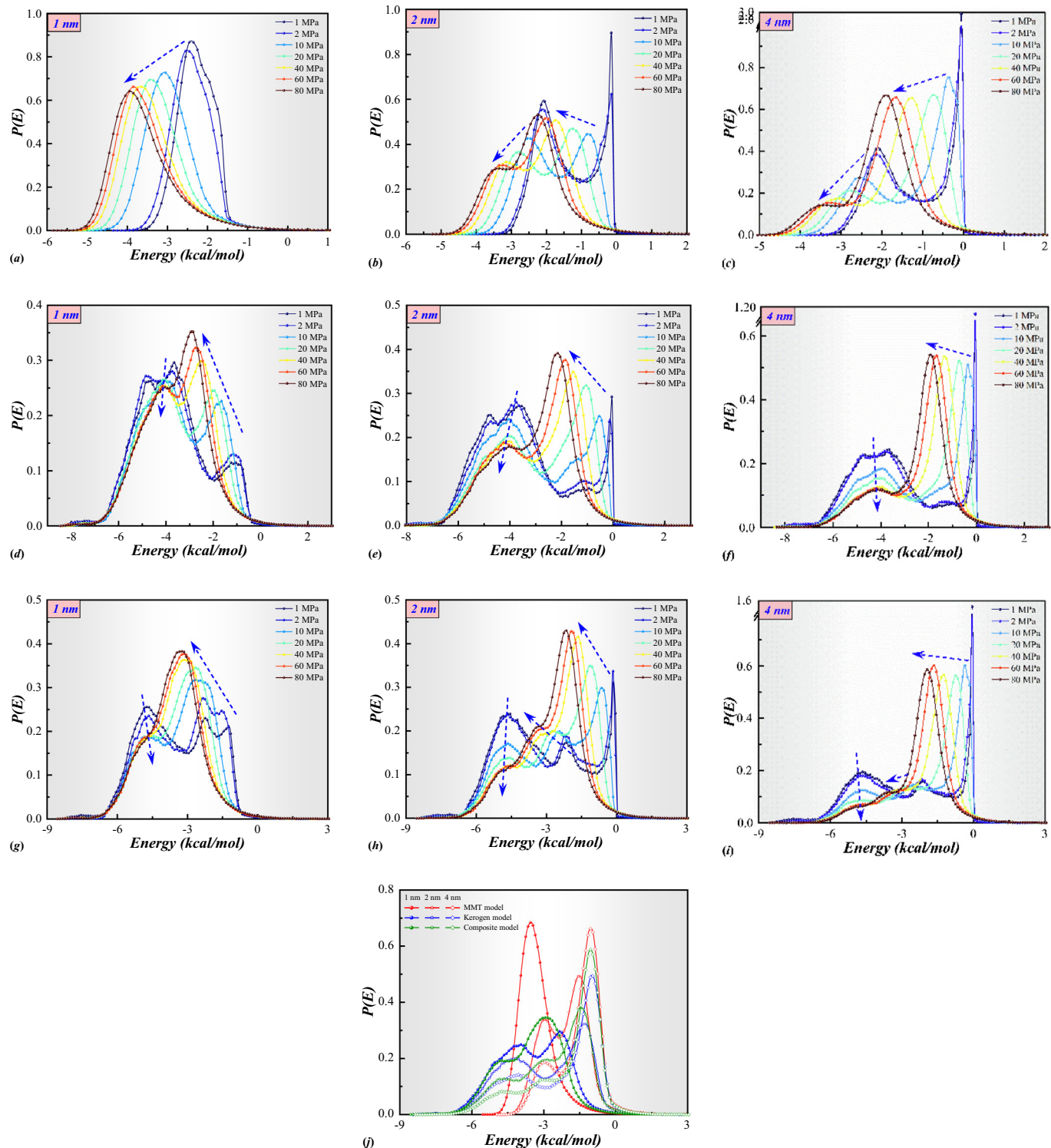


Fig. 11. Energy distribution of methane sorption in the three models with the apertures of 1, 2 and 4 nm, respectively. (a-c) MMT model. (d-f) Kerogen model. (g-i) MMT-kerogen composite model. (j) Variation of energy distribution curves with pore size in the three models at 30 MPa.

methane preferentially adsorbs in the smaller pores than in the larger pores.

4.1.4. Isosteric heat of methane sorption

During the isothermal sorption simulation, the gas molecules move to the solid surface under the action of pore wall forces, and the molecular motion speed is dramatically reduced, then the heat is released [76,77]. The magnitude of the isosteric heat

of sorption can reflect the strength of gas sorption [23,78,79]. The variation of the isosteric heat of sorption with pressure for different models and apertures is presented in Fig. 12. As illustrated in Fig. 12(a), the isosteric heat of sorption increases with increasing pressure in the MMT models, indicating that the sorption stability gradually increases. For kerogen and MMT-kerogen models, the isosteric heat of sorption tends to decrease sharply in the pressure range of 1–20 MPa, indicating that the sorption is in an extremely

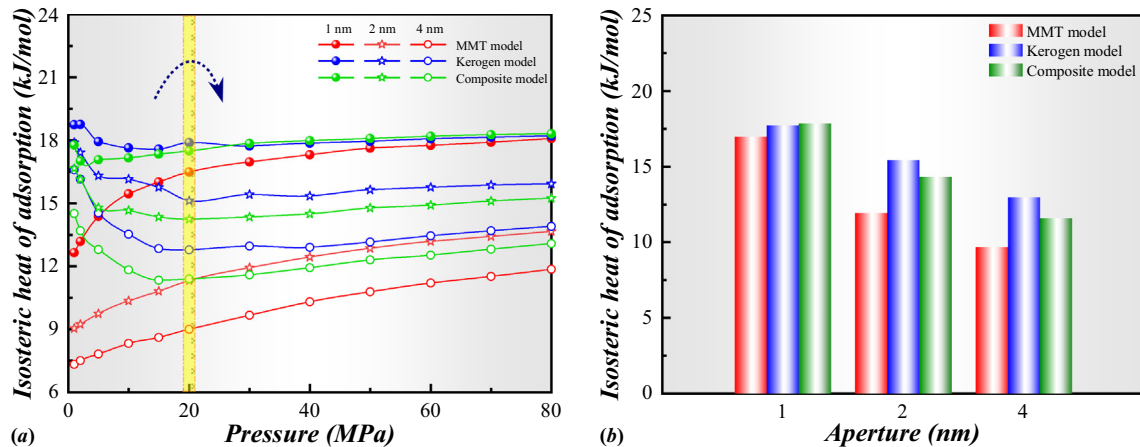


Fig. 12. Methane isosteric heat of adsorption. (a) Variation of methane isosteric heat of sorption with pressure for different models and pore sizes. (b) The relationship between methane isosteric heat of sorption and pore size for the three models at 30 MPa.

unstable state, which is also related to the inhomogeneity of the kerogen matrix. With the further increase of pressure, the isosteric heat of sorption showed a slowly increasing trend, suggesting that the sorption is more stable at this time. In addition, the isosteric heat of sorption is less than 42 kJ/mol in all three models, demonstrating that the sorption of methane on MMT and kerogen is physical sorption [48,80–82]. The relationship between the isosteric heat sorption and pore size at 30 MPa is shown in Fig. 12(b). It can be seen from the Fig. 12(b) that the isosteric heat of sorption decreases with the increase of aperture. This suggests that the sorption in smaller pores is more stable, which is because the interaction between methane in the center of the pore and MMT or kerogen is gradually weakened as the aperture increases. By comparing the isosteric heat of sorption for the same pressure and aperture, it can be found that the isosteric heat of sorption is the largest in the kerogen model, followed by the MMT-kerogen composite model and the smallest in the MMT model. This is due to the fact that in the model with kerogen matrix, methane will adsorb not only in the main pore, but also absorb in the kerogen matrix, which also demonstrated that the sorption performance of kerogen is stronger than that of MMT from another perspective.

4.2. Methane self-diffusion characteristics

Nanopore structure and pore surface properties have great influences on the gas sorption characteristics and have significant impacts on the diffusion. Self-diffusivity is a monomolecular property and is therefore sensitive to inter-fluid collisions and fluid-solid collisions. The translational self-diffusion coefficient can be obtained from the integration of the velocity autocorrelation function or the integration of the mean square displacement (MSD). In this study, the self-diffusion coefficient is calculated using the MSD according to the Einstein relation [39,83,84].

$$D = \frac{1}{6N} \lim_{t \rightarrow \infty} \frac{d}{dt} \left\langle \sum_{j=1}^N |\mathbf{r}_j(t) - \mathbf{r}_j(0)|^2 \right\rangle \quad (8)$$

where N is the number of particles, t is the time and r is the position of the particles. In the EMD simulation within the NVT ensemble, the MSD curve of the methane molecules is firstly obtained, and then a linear fitting is carried out. By fitting the slope of the line, the self-diffusion coefficient of the methane can be obtained.

4.2.1. Effect of pore size

The mean square displacement (MSD) curves and their fitting lines of methane in different models and pore sizes for different pressures (5, 50 MPa) are presented in Fig. S2(a, b, c) of the Supporting Information. It can be seen from the Fig. S2 that the simulation results and the fitting lines have a high agreement for all simulation cases. And the slope of the fitting lines decreases with the increase of pressure for the same aperture. The variation of the self-diffusion coefficient with pressure for the three models with different apertures is shown in Fig. 13. It can be seen from the Fig. 13 that the self-diffusion coefficient of methane decreases rapidly with increasing pressure and gradually stabilizes at the pressure greater than 20 MPa. This is because the collision between gas molecules is enhanced as the gas density increases with increasing pressure. Meanwhile, the collision between gas molecules and the pore wall is also enhanced, resulting in greater resistance to gas diffusion. In addition, the self-diffusion coefficient increases with increasing aperture. This is because the adsorption strength is weaker in larger pores, resulting in a lower gas density and a lower collision probability between gas molecules. Moreover, since the gas molecules near the pore center are farther away from the pore wall in larger pores, the collision probability between the gas molecules and the pore wall is also smaller, so larger pores are more conducive to the gas diffusion. Furthermore, we calculated the variation of the mean free path of methane with pressure for a given temperature condition (403.15 K). As illustrated in

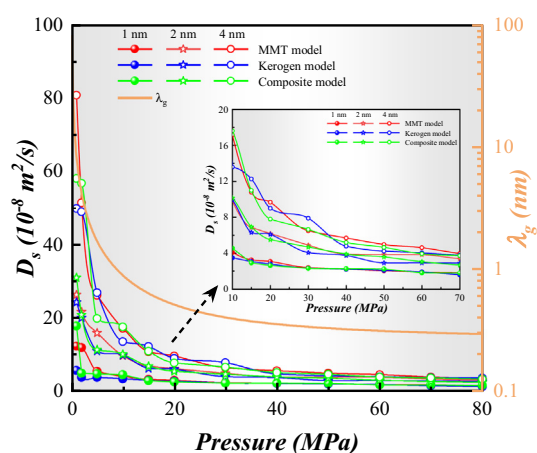


Fig. 13. Variation of methane self-diffusion coefficient and mean free path with pressure for the three models with different pore sizes.

Fig. 13, the self-diffusion coefficient has the consistent variation trend as the mean free path. This is because the mean free path between molecules decreases with the increase of pressure, so the diffusion is weakened. This explains the variation pattern of the self-diffusion in terms of collisions of gas molecules and collisions between gas molecules and pore walls.

4.2.2. Effect of pore surface properties

In order to further investigate the effect of pore surface properties on gas self-diffusion, firstly, we divided the methane in the 4 nm pores of the three models at 80 MPa into 10 bins from the bottom up, and the width of each bin was approximately equal to the diameter of methane molecules (3.8 Å). Then the self-diffusion coefficients of methane at different positions were investigated, and the results are presented in **Fig. 14(a)**. As illustrated in **Fig. 14(a)**, the self-diffusion coefficient of methane shows an approximately parabolic shape. This is because, firstly, the molecular density is higher near the pore wall than the center, which causes the collision between methane molecules to be more intense. Secondly, the methane molecules near the pore wall are more likely to collide with the pore wall during the diffusion process. In addition, in the kerogen model, the self-diffusion coefficient near the upper and lower of pore walls deviates because of the amorphous structure of kerogen molecules, which leads to the surface properties of the kerogen matrix in the upper and lower parts of the model can be different. Meanwhile, this phenomenon was also found in the MMT-kerogen composite nanopore, which is also related to the difference in surface properties. Furthermore, the self-diffusion coefficients of different adsorption layers in MMT-kerogen composite nanopores with varying apertures at 80 MPa were calculated, as shown in **Fig. 14(b)**. It can be observed from **Fig. 14(b)** that the self-diffusion coefficient of the first adsorption layer is always smaller than that of the second, the third adsorption layer is smaller than that of the fourth. In other words, the self-diffusion coefficient near kerogen at the same position from the pore wall is smaller than that of MMT. This is because during the model construction process, the surface of the generated kerogen matrix is uneven and has a large roughness due to the amorphous structure of the kerogen molecules compared to the MMT supercell structure. The surface roughness will produce a great resistance to the movement of gas, and thus hindering the diffusion. Besides, the self-diffusion coefficient of each adsorption layer increases with the increase of aperture for a similar reason as the analysis in the previous section.

5. Conclusions

In this work MMT unit cell and type IIA kerogen molecules were first employed to construct the MMT, kerogen and MMT-kerogen composite nanopores based on the result observed by scanning electron microscopy. In addition, we validated the accuracy of the constructed kerogen matrix model and the force field used, which shown a good agreement with previous studies. Then isothermal sorption and self-diffusion of methane in the three kinds of nanopores were simulated by a series of GCMC and EMD methods. The main conclusions drawn are as follows.

1. The absolute adsorption amount of methane in nanopores of the three models increases continuously with increasing pressure and gradually reaches adsorption saturation. Smaller pores have stronger gas adsorption capacity. MMT surface has a stronger adsorption performance than kerogen in single nanopores. But the kerogen matrix has a larger methane sorption capacity per unit mass than MMT due to its larger specific surface area. The absolute adsorption in the MMT and kerogen nanopores with pressure can be well fitted by Langmuir isothermal adsorption.
2. Methane molecules will adsorb on the surface of MMT and kerogen to form adsorption layers. The double adsorption layer formed in the 1 nm pores basically occupies the pore interspace, while the quadruple adsorption layer structure formed in the 2 and 4 nm pores. The surface adsorption difference between MMT and kerogen is smaller in the smaller aperture composite nanopores.
3. Methane adsorption in nanopores is more stable at higher pressure from the perspective of sorption energy distribution, and methane molecules preferentially adsorb in smaller pores. The isosteric heat of methane sorption decreases with increasing aperture, indicating that methane adsorption is more stable in smaller pores.
4. The self-diffusion of methane in nanopores is mainly influenced by intermolecular collisions and collisions between molecules and pore walls. The self-diffusion coefficient of methane decreases with increasing pressure. The pore surface roughness will impede the self-diffusion of gas, and the degree of the hindrance of the self-diffusion is more significant on the surface of kerogen than MMT.

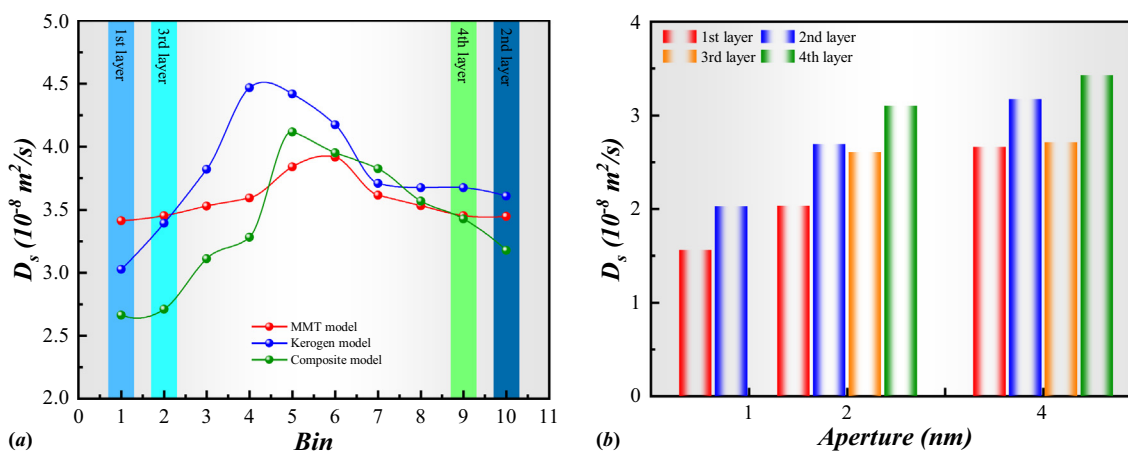


Fig. 14. Self-diffusion coefficient of methane in three models at 80 MPa. (a) Variation of methane self-diffusion coefficient in three models of 4 nm with the location at 80 MPa. (b) Methane self-diffusion coefficient of each gas adsorption layer in different aperture MMT-kerogen models at 80 MPa.

CRediT authorship contribution statement

Fangtao Lyu: Methodology, Formal analysis, Writing – original draft, Visualization. **Zhengfu Ning:** Writing – review & editing, Supervision, Validation, Funding acquisition. **Shanshan Yang:** Writing – review & editing. **Zhongqi Mu:** Writing – review & editing. **Zhilin Cheng:** Writing – review & editing. **Zhipeng Wang:** Writing – review & editing. **Bei Liu:** Writing – review & editing.

Declaration of Competing Interest

The authors declare that they have no known competing financial interests or personal relationships that could have appeared to influence the work reported in this paper.

Acknowledgements

This work was supported by the National Natural Science Foundation of China (Grant Nos 51774298 and 51974330) and the Joint Funds of the National Natural Science Foundation of China (Grant No. U19B6003-03-04). Moreover, the authors would like to thanks all anonymous reviewers for their extremely helpful suggestions and comments.

Appendix A. Supplementary material

Supplementary data to this article can be found online at <https://doi.org/10.1016/j.molliq.2022.119263>.

References

- [1] Y. Gensterblum, A. Ghanizadeh, R.J. Cuss, A. Amann-Hildenbrand, B.M. Krooss, C.R. Clarkson, J.F. Harrington, M.D. Zoback, Gas transport and storage capacity in shale gas reservoirs – A review. Part A: Transport processes. *Journal of Unconventional Oil and Gas, Resources* 12 (2015) 87–122.
- [2] C. Afagwu, M.A. Mahmoud, S. Alafnan, S. Patil, Multiscale storage and transport modeling in unconventional shale gas: A review, *J. Petrol. Sci. Eng.* 208 (2022) 109518.
- [3] S. Akilu, E. Padmanabhan, Z. Sun, A review of transport mechanisms and models for unconventional tight shale gas reservoir systems, *Int. J. Heat Mass Transf.* 175 (2021) 121125.
- [4] F. Lyu, Z. Ning, X. Wu, Q. Wang, K. Gu, Z. Cheng, Z. Mu, A comparative study of gas transport in dry and moisturized shale matrix considering organic matter volume fraction and water distribution characteristics, *J. Petrol. Sci. Eng.* 208 (2022) 109483.
- [5] S. Das, J. Adeoye, I. Dhiman, H.Z. Bilheux, B.R. Ellis, Imbibition of Mixed-Charge Surfactant Fluids in Shale Fractures, *Energy Fuels* 33 (4) (2019) 2839–2847.
- [6] L. Ran, Li. Gaomin, Z. Jinzhou, R. Lan, W.u. Jianfa, Productivity model of shale gas fractured horizontal well considering complex fracture morphology, *J. Petrol. Sci. Eng.* 208 (2022) 109511.
- [7] S. Zhang, J. Yan, J. Cai, X. Zhu, Q. Hu, M. Wang, B. Geng, G. Zhong, Fracture characteristics and logging identification of lacustrine shale in the Jiayang Depression, Bohai Bay Basin Eastern China, *Mar. Petrol. Geol.* 132 (2021) 105192.
- [8] R. Feng, S. Chen, S. Bryant, J. Liu, Stress-dependent permeability measurement techniques for unconventional gas reservoirs: Review, evaluation, and application, *Fuel* 256 (2019) 115987.
- [9] X. Wu, Z. Ning, R. Qi, Q. Wang, L. Huang, Pore Characterization and Inner Adsorption Mechanism Investigation for Methane in Organic and Inorganic Matters of Shale, *Energy Fuels* 34 (4) (2020) 4106–4115.
- [10] K. Zhang, X. Li, Y. Wang, W. Liu, Y. Yu, L. Zhou, W. Feng, Paleo-environments and organic matter enrichment in the shales of the Cambrian Niutitang and Wunitang Formations, south China: Constraints from depositional environments and geochemistry, *Mar. Pet. Geol.* 134 (2021) 105329.
- [11] L. Zhang, D. Xiao, S. Lu, S. Jiang, S. Lu, Effect of sedimentary environment on the formation of organic-rich marine shale: Insights from major/trace elements and shale composition, *Int. J. Coal Geol.* 204 (2019) 34–50.
- [12] X.-J. Wu, Z.-F. Ning, Z.-L. Cheng, Q. Wang, R.-R. Qi, L. Huang, W.-T. Zhang, Simplified local density model for gas adsorption in cylindrical carbon pores, *Appl. Surf. Sci.* 491 (2019) 335–349.
- [13] Z. Pan, L.D. Connell, Reservoir simulation of free and adsorbed gas production from shale, *J. Nat. Gas Sci. Eng.* 22 (2015) 359–370.
- [14] Y. Xia, Y. Jin, K.P. Chen, M. Chen, D. Chen, Simulation on gas transport in shale: The coupling of free and adsorbed gas, *J. Nat. Gas Sci. Eng.* 41 (2017) 112–124.
- [15] L. Huang, W. Zhou, H. Xu, L.u. Wang, J. Zou, Q. Zhou, Dynamic fluid states in organic-inorganic nanocomposite: Implications for shale gas recovery and CO₂ sequestration, *Chem. Eng. J.* 411 (2021) 128423.
- [16] F. Yang, Z. Ning, Q. Wang, R. Zhang, B.M. Krooss, Pore structure characteristics of lower Silurian shales in the southern Sichuan Basin, China: Insights to pore development and gas storage mechanism, *Int. J. Coal Geol.* 156 (2016) 12–24.
- [17] F. Yang, Z. Ning, Q. Wang, H. Liu, Pore structure of Cambrian shales from the Sichuan Basin in China and implications to gas storage, *Mar. Pet. Geol.* 70 (2016) 14–26.
- [18] S. Chen, J. Jiang, B.o. Guo, A pore-network-based upscaling framework for the nanoconfined phase behavior in shale rocks, *Chem. Eng. J.* 417 (2021) 129210.
- [19] R. Qi, Z. Ning, Q. Wang, L. Huang, X. Wu, Z. Cheng, W. Zhang, Measurements and modeling of high-pressure adsorption of CH₄ and CO₂ on shales, *Fuel* 242 (2019) 728–743.
- [20] R. Qi, Z. Ning, Q. Wang, Y. Zeng, L. Huang, S. Zhang, H. Du, Sorption of Methane, Carbon Dioxide, and Their Mixtures on Shales from Sichuan Basin, China, *Energy Fuels* 32 (3) (2018) 2926–2940.
- [21] L. Huang, Z. Ning, H. Lin, W. Zhou, Lu. Wang, J. Zou, H. Xu, High-Pressure Sorption of Methane, Ethane, and Their Mixtures on Shales from Sichuan Basin, China, *Energy Fuels* 35 (5) (2021) 3989–3999.
- [22] R. Hu, W. Wang, J. Tan, L. Chen, J. Dick, G. He, Mechanisms of shale gas adsorption: Insights from a comparative study on a thermodynamic investigation of microfossil-rich shale and non-microfossil shale, *Chem. Eng. J.* 411 (2021) 128463.
- [23] W. Dang, J. Zhang, H. Nie, F. Wang, X. Tang, N. Wu, Q. Chen, X. Wei, R. Wang, Isotherms, thermodynamics and kinetics of methane-shale adsorption pair under supercritical condition: Implications for understanding the nature of shale gas adsorption process, *Chem. Eng. J.* 383 (2020) 123191.
- [24] D.J.K. Ross, B.R. Marc, The importance of shale composition and pore structure upon gas storage potential of shale gas reservoirs, *Mar. Pet. Geol.* 26 (6) (2009) 916–927.
- [25] M. Gasparik, P. Bertier, Y. Gensterblum, A. Ghanizadeh, B.M. Krooss, R. Little, Geological controls on the methane storage capacity in organic-rich shales, *Int. J. Coal Geol.* 123 (2014) 34–51.
- [26] L. Huang, A. Khoshnood, A. Firoozabadi, Swelling of Kimmeridge kerogen by normal-alkanes, naphthenes and aromatics, *Fuel* 267 (2020) 117155.
- [27] S. Alafnan, A. Awotunde, G. Glatz, S. Adjei, I. Alrumaih, A. Gowida, Langmuir adsorption isotherm in unconventional resources: Applicability and limitations, *J. Petrol. Sci. Eng.* 207 (2021) 109172.
- [28] S. Alafnan, Petrophysics of Kerogens Based on Realistic Structures, *ACS Omega* 6 (14) (2021) 9549–9558.
- [29] L. Huang, Z. Ning, Q. Wang, R. Qi, Z. Cheng, X. Wu, W. Zhang, H. Qin, Kerogen deformation upon CO₂/CH₄ competitive sorption: Implications for CO₂ sequestration and enhanced CH₄ recovery, *J. Petrol. Sci. Eng.* 183 (2019) 106460.
- [30] L. Huang, Z. Ning, Q. Wang, R. Qi, Z. Cheng, X. Wu, W. Zhang, H. Qin, Molecular Insights into Kerogen Deformation Induced by CO₂/CH₄ Sorption: Effect of Maturity and Moisture, *Energy Fuels* 33 (6) (2019) 4792–4805.
- [31] Horn AD, Breakthrough Mobile Water Treatment Converts 75% of Fracturing Flowback Fluid to Fresh Water and Lowers CO₂ Emissions. *SPE Americas E&P Environmental and Safety Conference*. 2009.
- [32] J. Bai, Y. Kang, M. Chen, Z. Chen, L. You, Impact of the Water Adsorption Monolayer on Methane Ad-/Desorption Behavior in Gas Shale Nanopores, *Ind. Eng. Chem. Res.* 60 (7) (2021) 3130–3141.
- [33] M. Wang, Q. Yu, Comparing the permeability of dry and moisturized crushed shales determined by the dynamic process data of methane adsorption, *J. Hydrol.* 590 (2020) 125375.
- [34] R. Yang, A. Jia, S. He, Q. Hu, M. Sun, T. Dong, Y. Hou, S. Zhou, Experimental investigation of water vapor adsorption isotherm on gas-producing Longmaxi shale: Mathematical modeling and implication for water distribution in shale reservoirs, *Chem. Eng. J.* 406 (2021) 125982.
- [35] F. Yang, B. Lyu, S. Xu, Water Sorption and Transport in Shales: An Experimental and Simulation Study, *Water Resour. Res.* 57 (2) (2021).
- [36] X. Ma, H. Wang, S. Zhou, Z. Shi, L. Zhang, Deep shale gas in China: Geological characteristics and development strategies, *Energy Rep.* 7 (2021) 1903–1914.
- [37] H. Wen, M. Chen, Y. Jin, Y. Zhang, W. Ge, J. Du, C. Zeng, Water activity characteristics of deep brittle shale from Southwest China, *Appl. Clay Sci.* 108 (2015) 165–172.
- [38] Y.u. Sun, M. Wu, T. Tong, P. Liu, P. Tang, Z. Gan, P. Yang, Q. He, B. Liu, Organic compounds in Weiyuan shale gas produced water: Identification, detection and rejection by ultrafiltration-reverse osmosis processes, *Chem. Eng. J.* 412 (2021) 128699.
- [39] H. Sun, W. Sun, H. Zhao, Y. Sun, D. Zhang, X. Qi, Y. Li, Adsorption properties of CH₄ and CO₂ in quartz nanopores studied by molecular simulation, *RSC Adv.* 6 (39) (2016) 32770–32778.
- [40] S. Wang, Q. Feng, F. Javadpour, Q. Hu, K. Wu, Competitive adsorption of methane and ethane in montmorillonite nanopores of shale at supercritical conditions: A grand canonical Monte Carlo simulation study, *Chem. Eng. J.* 355 (2019) 76–90.
- [41] S. Zhan, Y. Su, M. Lu, M. Cai, J. Fu, Z. Liu, K. Wang, Q.i. Han, G. Li, Effect of Surface Type on the Flow Characteristics in Shale Nanopores, *Geofluids* 2021 (2021) 1–12.
- [42] L. Huang, Z. Ning, Q. Wang, H. Ye, Z. Wang, Z. Sun, H. Qin, Microstructure and adsorption properties of organic matter in Chinese Cambrian gas shale: Experimental characterization, molecular modeling and molecular simulation, *Int. J. Coal Geol.* 198 (2018) 14–28.

- [43] C. Afagwu, S. Al-Afnan, S. Patil, J. Aljaberi, M.A. Mahmoud, J. Li, The impact of pore structure and adsorption behavior on kerogen tortuosity, *Fuel* 303 (2021) 121261.
- [44] F. Guo, S. Wang, Q. Feng, X. Yao, Q. Xue, X. Li, Adsorption and absorption of supercritical methane within shale kerogen slit, *J. Mol. Liq.* 320 (2020) 114364.
- [45] W. Pang, Y. He, C. Yan, Z. Jin, Tackling the challenges in the estimation of methane absolute adsorption in kerogen nanoporous media from molecular and analytical approaches, *Fuel* 242 (2019) 687–698.
- [46] P. Ungerer, J. Collell, M. Yiannourakou, Molecular Modeling of the Volumetric and Thermodynamic Properties of Kerogen: Influence of Organic Type and Maturity, *Energy Fuels* 29 (1) (2015) 91–105.
- [47] J. Zhou, Q. Mao, K.H. Luo, Effects of Moisture and Salinity on Methane Adsorption in Kerogen: A Molecular Simulation Study, *Energy Fuels* 33 (6) (2019) 5368–5376.
- [48] L. Huang, Z. Ning, Q. Wang, W. Zhang, Z. Cheng, X. Wu, H. Qin, Effect of organic type and moisture on CO₂/CH₄ competitive adsorption in kerogen with implications for CO₂ sequestration and enhanced CH₄ recovery, *Appl. Energy* 210 (2018) 28–43.
- [49] G. Berghe, S. Kline, S. Burkett, L. Bivens, D. Johnson, R. Singh, Effect of CO₂ and H₂O on the behavior of shale gas confined inside calcite [104] slit-like nanopore: a molecular dynamics simulation study, *J. Mol. Model.* 25 (9) (2019).
- [50] X. Yu, J. Li, Z. Chen, K. Wu, L. Zhang, G. Hui, M. Yang, Molecular dynamics computations of brine-CO₂/CH₄-shale contact angles: Implications for CO₂ sequestration and enhanced gas recovery, *Fuel* 280 (2020) 118590.
- [51] Jin H, Sonnenberg SA. Characterization for Source Rock Potential of the Bakken Shales in the Williston Basin, North Dakota and Montana. SPE/AAPG/SEG Unconventional Resources Technology Conference. 2013:URTEC-1581243-MS.
- [52] J. Collell, P. Ungerer, G. Galliero, M. Yiannourakou, F. Montel, M. Pujo, Molecular Simulation of Bulk Organic Matter in Type II Shales in the Middle of the Oil Formation Window, *Energy Fuels* 28 (12) (2014) 7457–7466.
- [53] K.S. Okiongbo, A.C. Aplin, S. Larter, Changes in Type II Kerogen Density as a Function of Maturity: Evidence from the Kimmeridge Clay Formation, *Energy Fuels* 19 (2005) 2495–2499.
- [54] J. Zhou, Z. Jin, K.H. Luo, Effects of Moisture Contents on Shale Gas Recovery and CO₂ Sequestration, *Langmuir* 35 (26) (2019) 8716–8725.
- [55] Z. Sun, X. Li, W. Liu, T. Zhang, M. He, H. Nasrabadi, Molecular dynamics of methane flow behavior through realistic organic nanopores under geologic shale condition: Pore size and kerogen types, *Chem. Eng. J.* 398 (2020) 124341.
- [56] N.T. Skipper, F.-R.-C. Chang, G. Sposito, Monte Carlo Simulation of Interlayer Molecular Structure in Swelling Clay Minerals. 1. Methodology, *Clays Clay Miner.* 43 (3) (1995) 285–293.
- [57] Q. Wang, L. Huang, Molecular insight into competitive adsorption of methane and carbon dioxide in montmorillonite: Effect of clay structure and water content, *Fuel* 239 (2019) 32–43.
- [58] H. Sun, COMPASS: An ab Initio Force-Field Optimized for Condensed-Phase ApplicationsOverview with Details on Alkane and Benzene Compounds, *J. Phys. Chem. B* 102 (1998) 7338–7364.
- [59] L. Yang, X. Zhou, K. Zhang, F. Zeng, Z. Wang, Investigation of dynamical properties of methane in slit-like quartz pores using molecular simulation, *RSC Adv.* 8 (59) (2018) 33798–33816.
- [60] Z. Peng, C.S. Ewig, M.-J. Hwang, M. Waldman, A.T. Hagler, Derivation of Class II Force Fields. 4. van der Waals Parameters of Alkali Metal Cations and Halide Anions, *J. Phys. Chem. A* 101 (39) (1997) 7243–7252.
- [61] Y. Li, Z. Hu, X. Liu, S. Gao, X. Duan, J. Chang, J. Wu, Insights into interactions and microscopic behavior of shale gas in organic-rich nano-slits by molecular simulation, *J. Nat. Gas Sci. Eng.* 59 (2018) 309–325.
- [62] S. Wang, X. Yao, Q. Feng, F. Javadpour, Y. Yang, Q. Xue, X. Li, Molecular insights into carbon dioxide enhanced multi-component shale gas recovery and its sequestration in realistic kerogen, *Chem. Eng. J.* 425 (2021) 130292.
- [63] N. Metropolis, A.W. Rosenbluth, M.N. Rosenbluth, A.H. Teller, E. Teller, Equation of state calculations by fast computing machines, *J. Chem. Phys.* 21 (6) (1953) 1087–1092.
- [64] Averill JD, Reneke P, Peacock RD. National Institute of Standards and Technology (NIST). 2004.
- [65] S. Brandani, E. Mangano, L. Sarkisov, Net, excess and absolute adsorption and adsorption of helium, *Adsorption* 22 (2) (2016) 261–276.
- [66] O. Talu, A.L. Myers, Molecular simulation of adsorption: Gibbs dividing surface and comparison with experiment, *AIChE J.* 47 (5) (2001) 1160–1168.
- [67] Y. Tian, C. Yan, Z. Jin, Characterization of Methane Excess and Absolute Adsorption in Various Clay Nanopores from Molecular Simulation, *Sci. Rep.* 7 (1) (2017).
- [68] Stukowski A. Visualization and analysis of atomistic simulation data with OVITO the Open Visualization Tool. *Modelling Simulation in Materials Science Engineering* 2009;18:015012.
- [69] M.L. Connolly, Solvent-accessible surfaces of proteins and nucleic acids, *Science* 221 (4612) (1983) 709–713.
- [70] T. Cao, Z. Song, S. Wang, J. Xia, A comparative study of the specific surface area and pore structure of different shales and their kerogens, *Sci. China Earth Sci.* 58 (4) (2015) 510–522.
- [71] S. Alafnan, Utilization of supercritical carbon dioxide for mechanical degradation of organic matters contained in shales, *Fuel* 316 (2022) 123427.
- [72] T.F.T. Rexer, M.J. Benham, A.C. Aplin, K.M. Thomas, Methane Adsorption on Shale under Simulated Geological Temperature and Pressure Conditions, *Energy Fuels* 27 (6) (2013) 3099–3109.
- [73] T.F. Rexer, E.J. Mathia, A.C. Aplin, K.M. Thomas, High-pressure methane adsorption and characterization of pores in Posidonia shales and isolated kerogens, *Energy Fuels* 28 (5) (2014) 2886–2901.
- [74] J. Xie, Y. Liang, Q. Zou, Z. Wang, X. Li, Prediction Model for Isothermal Adsorption Curves Based on Adsorption Potential Theory and Adsorption Behaviors of Methane on Granular Coal, *Energy Fuels* 33 (3) (2019) 1910–1921.
- [75] P. Cosoli, M. Ferrone, S. Priol, M. Fermeglia, Hydrogen sulphide removal from biogas by zeolite adsorption: Part I GCMC molecular simulations, *Chem. Eng. J.* 145 (1) (2008) 86–92.
- [76] Z. Mu, Z. Ning, C. Ren, Methane adsorption on shales and application of temperature-related composite models based on dual adsorption modes, *J. Petrol. Sci. Eng.* 208 (2022) 109379.
- [77] J. Deng, J. Kang, F. Zhou, H. Li, D. Zhang, G. Li, The adsorption heat of methane on coal: Comparison of theoretical and calorimetric heat and model of heat flow by microcalorimeter, *Fuel* 237 (2019) 81–90.
- [78] D. Liu, Z. Zou, Y. Cai, Y. Qiu, Y. Zhou, S. He, An updated study on CH₄ isothermal adsorption and isosteric adsorption heat behaviors of variable rank coals, *J. Nat. Gas Sci. Eng.* 89 (2021) 103899.
- [79] L. Chen, L. Zuo, Z. Jiang, S. Jiang, K. Liu, J. Tan, L. Zhang, Mechanisms of shale gas adsorption: Evidence from thermodynamics and kinetics study of methane adsorption on shale, *Chem. Eng. J.* 361 (2019) 559–570.
- [80] T. Wang, S. Tian, G. Li, M. Sheng, Selective adsorption of supercritical carbon dioxide and methane binary mixture in shale kerogen nanopores, *J. Nat. Gas Sci. Eng.* 50 (2018) 181–188.
- [81] Q. Sun, W. Liu, N.a. Zhang, Molecular insights into recovery of shale gas by CO₂ injection in kerogen slit nanopores, *J. Nat. Gas Sci. Eng.* 90 (2021) 103903.
- [82] J. Xiong, X. Liu, L. Liang, Q. Zeng, Adsorption of methane in organic-rich shale nanopores: An experimental and molecular simulation study, *Fuel* 200 (2017) 299–315.
- [83] S. Tesson, A. Firroozabadi, Methane Adsorption and Self-Diffusion in Shale Kerogen and Slat Nanopores by Molecular Simulations, *J. Phys. Chem. C* 122 (41) (2018) 23528–23542.
- [84] S. Wang, Q. Feng, M. Zha, F. Javadpour, Q. Hu, Supercritical Methane Diffusion in Shale Nanopores: Effects of Pressure, Mineral Types, and Moisture Content, *Energy Fuels* 32 (1) (2018) 169–180.